energies

MDPI

Article

PSO Self-Tuning Power Controllers for Low Voltage Improvements of an Offshore Wind Farm in Taiwan

Yu-Hsiang Hung, Yi-Wei Chen, Cheng-Han Chuang and Yuan-Yih Hsu *

Department of Electrical Engineering, National Taiwan University, EE Building 2, No. 1, Sec. 4, Roosevelt Rd., Taipei City 106, Taiwan; ken0911949533@gmail.com (Y.-H.H.); r06921069@ntu.edu.tw (Y.-W.C.); r09921087@g.ntu.edu.tw (C.-H.C.)

* Correspondence: hsuyy@ntu.edu.tw

Abstract: A de-loaded real power control strategy is proposed to decrease the real power output and increase the reactive power output of a grid-connected offshore wind farm in order to improve the voltage profile when the wind farm is subject to a grid fault. A simplified linear model of the wind farm is first derived and a fixed-gain proportional-integral (PI) real power controller is designed based on the pole-zero cancellation method. To improve the dynamic voltage response when the system is subject to a major disturbance such as a three-phase fault in the grid, a self-tuning controller based on particle swarm optimization (PSO) is proposed to adapt the PI controller gains based on the on-line measured system variables. Digital simulations using MATLAB/SIMULINK were performed on an offshore wind farm connected to the power grid in central Taiwan in order to validate the effectiveness of the proposed PSO controller. It is concluded from the simulation results that a better dynamic voltage response can be achieved by the proposed PSO self-tuning controller than the fixed-gain controller when the grid is subject to a three-phase fault. In addition, low voltage ride through (LVRT) requirements of the local utility can be met by the wind farm with the proposed power controller.

Keywords: doubly fed induction generator; low voltage ride through; particle swarm optimization; real and reactive power control; rotor side converter; self-tuning controller; wind farm

Citation: Hung, Y.-H.; Chen, Y.-W.; Chuang, C.-H.; Hsu, Y.-Y. PSO Self-Tuning Power Controllers for Low Voltage Improvements of an Offshore Wind Farm in Taiwan. *Energies* **2021**, *14*, 6670. https://doi.org/10.3390/en14206670

Academic Editors: Olimpo Anaya-Lara and John Olav Giæver Tande

Received: 27 August 2021
Accepted: 12 October 2021
Published: 14 October 2021

1. Introduction

According to the nuclear-free energy policy in Taiwan, more than 20% of the electrical energy will come from renewable energy by 2025. Furthermore, the installed capacities of the island and offshore wind farms will reach 1.2 GW and 5.7 GW, respectively. With the increasing percentage of wind power generation, how to improve the fault ride through (FRT) capability of a wind farm when it is subject to a grid fault very close to the wind farm has received much attention in recent years [1].

Doubly fed induction generators (DFIGs) have been widely employed for wind energy conversion due to their variable speed operation capability, low converter cost, and independent controllability of real and reactive power. However, the DFIG is sensitive to grid voltage variations as its stator is directly connected to the grid [2–4]. Numerous papers have been published to protect the DFIG and the power electronic devices in the rotor side converter (RSC) and grid side converter (GSC) from over-current and over-voltage under disturbance conditions [5–21]. A rotor side crowbar circuit [5,6] has been proposed to divert transient rotor over-currents to prevent the RSC power semiconductor devices from being damaged under grid fault conditions. A DC-link brake chopper across the converter dc link was presented in [7] to ensure satisfactory dc link voltage during a fault. In [8], a series dynamic resistor (SDR) combined with a crowbar resistor and a DC-link brake chopper was designed. A proper value for the SDR was derived. A series voltage compensator in the stator was proposed in [9] to provide the required compensation voltage such that rotor over-current could be avoided. In [10], a dc-link chopper-controlled braking resistor and a

series dynamic braking resistor were studied. A passive resistive network consisting of shunt and series elements was installed at the stator [11,12] in order to achieve grid-fault tolerant operation. In [13], a protection scheme using series dynamic braking resistor was proposed to reach a desirable terminal voltage under voltage dip conditions. Grid side dynamic voltage restorers have been proposed in [14–17] to avoid rotor over-current and provide voltage support for the stator voltage. Although the aforementioned works are effective in protecting the DFIG and the associated power electronic devices under grid fault conditions, additional hardware components are required in order to implement these fault ride through techniques.

Another way to attain an improved fault ride through operation of DFIG is the software improvement and control algorithm method which requires no additional cost. In [22], a virtual damping strategy was proposed to control the stator transient flux under disturbance conditions. A control strategy that temporarily stored the output power in the generator rotor during grid faults was presented in [23] in which a pitch angle control was activated when the rotor speed exceeds its upper limit. In [24], a fuzzy controller was designed to control the real and reactive powers of the wind farm in order to maintain constant voltage at the point of common coupling (*PCC*). An optimal controller designed using a genetic algorithm was proposed in [25] to prevent over-currents during faults.

In this paper, a novel de-loaded power control algorithm without additional hardware components is proposed to improve the terminal voltage and to increase the reactive power output of a DFIG subject to grid faults. When a low voltage is detected at the DFIG stator, the real power command P_e^* is de-loaded from maximum power point tracking (MPPT) value to a level proportional to terminal voltage. After a simplified linear model of the wind farm is derived, a fixed-gain proportional-integral power controller is designed based on pole-zero cancellation method to yield the desired quadrature axis (q-axis) rotor current command i_{qr}^* from the real power command. To prevent rotor current from overloading, the direct axis (d-axis) rotor current command i_{dr}^* is selected such that the rotor current is equal to its rated value (1 pu). By decreasing the real power command P_e^* and q-axis rotor current command i_{qr}^*, the d-axis rotor current command i_{dr}^* and the reactive power output of DFIG can be increased. As a result, the terminal voltage is improved. Since the gains for the fixed-gain proportional-integral (PI) controllers have been designed based on a particular operating point, the dynamic responses of the PI controller may deteriorate when there is a drastic change in system variables due to a major disturbance such as a three-phase fault in the grid. In this work, a self-tuning controller based on particle swarm optimization (PSO) [26–28] is presented to adapt the real power controller gains K_p and K_i in real-time.

MATLAB/SIMULINK was employed to simulate the dynamic performance of an offshore wind farm connected to the power grid in central Taiwan under grid fault conditions. The simulation results indicate the proposed PSO self-tuning power controller can reach better voltage profile than the fixed-gain PI controller. It is also observed that the wind farm with the proposed controller meets the low voltage ride through (LVRT) requirements of the local utility in Taiwan. Based on the simulation results, it is concluded that a better voltage profile can be achieved by the proposed PSO self-tuning power controller than the fixed-gain PI controller. It is also observed from the simulation results that the wind farm with the proposed controller meets the low voltage ride through (LVRT) requirements of the local utility in Taiwan.

2. System Model

The system under study is an offshore wind farm connected to the utility grid in central Taiwan as shown in Figure 1.

The wind farm comprises 80 wind generators, each rated 2.5 MW. These wind generators are lumped as an equivalent 200 MW DFIG generator in order to reduce the computational burden of MATLAB/SIMULINK simulations. In addition, the system beyond Chung-Liao South substation is modeled as an infinite bus since its capacity is much

higher than the wind farm. As a result, only the portion of the system surrounded by the dashed line in Figure 1 is simulated by MATLAB/SIMULINK.

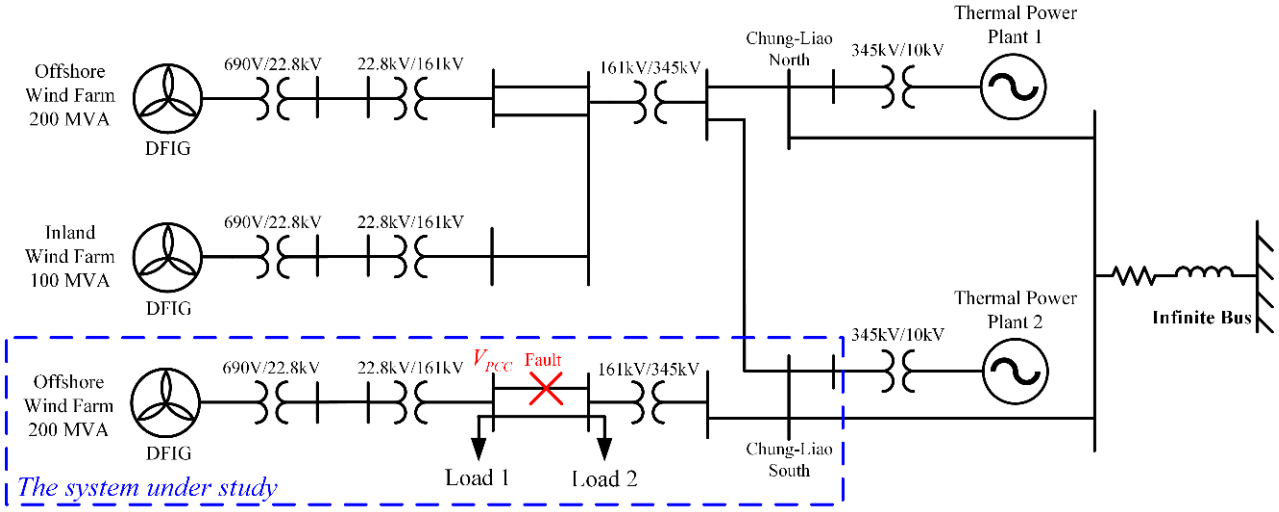

Figure 1. An offshore wind farm connected to the utility grid in central Taiwan.

The real and reactive power outputs of the wind farm are controlled by the RSC. By aligning the *d*-axis to stator flux linkage, the real power is controlled by the *q*-axis rotor current i_{qr} while the reactive power is controlled by the *d*-axis rotor current i_{dr} [29,30].

Figure 2 depicts the functional block diagram for real and reactive power control of a DFIG using a *dq*-axis rotor current regulator. As shown in Figure 2, a wind turbine simulator is employed to yield the DFIG mechanical torque T_m and mechanical power P_m under the specified wind speed V_w and rotor speed ω_r.

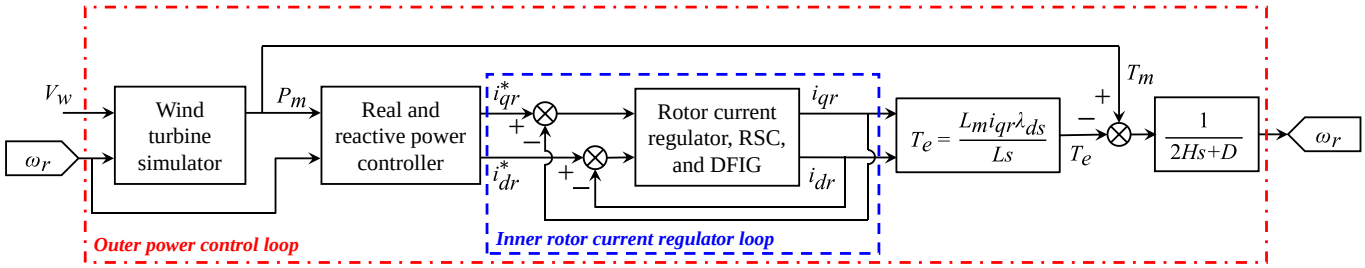

Figure 2. Functional block diagram for real and reactive power control of a doubly fed induction generator (DFIG).

2.1. Non-Linear Model of the Doubly Fed Induction Generator (DFIG) Current Regulator

Under stator flux orientation, the DFIG state equations with stator flux variations being considered can be written as follows [29].

$$\frac{d}{dt}\begin{bmatrix} i_{dr} \\ i_{qr} \\ \lambda_{ds} \end{bmatrix} = \begin{bmatrix} \frac{-(R_r+L_m^2 R_s/L_s^2)}{\sigma L_r} & \omega_{slip} & \frac{L_m R_s}{\sigma L_r L_s^2} \\ -\omega_{slip} & -\frac{R_r}{\sigma L_r} & -\frac{\omega_{slip} L_m}{\sigma L_r L_S} \\ \frac{L_m}{L_S} R_s & 0 & -\frac{R_s}{L_S} \end{bmatrix} \begin{bmatrix} i_{dr} \\ i_{qr} \\ \lambda_{ds} \end{bmatrix} + \begin{bmatrix} \frac{v_{dr}}{\sigma L_r} - \frac{L_m v_{ds}}{\sigma L_r L_s} \\ \frac{v_{qr}}{\sigma L_r} \\ v_{ds} \end{bmatrix} \quad (1)$$

To achieve *dq*-axis decoupling, feed-forward compensators are included in the *d*-axis and *q*-axis current regulators as described below:

$$v_{dr} = x_{dr} + \frac{L_m}{L_s}(v_{ds} - \frac{\lambda_{ds}}{L_s} R_s) - \omega_{slip} \sigma L_r i_{qr} \quad (2)$$

$$v_{qr} = x_{qr} + \omega_{slip}(\frac{L_m}{L_s}\lambda_{ds} + \sigma L_r i_{dr}) \quad (3)$$

where x_{dr} and x_{qr} are the d-axis and q-axis control signal from the PI current regulators as shown in Figure 3.

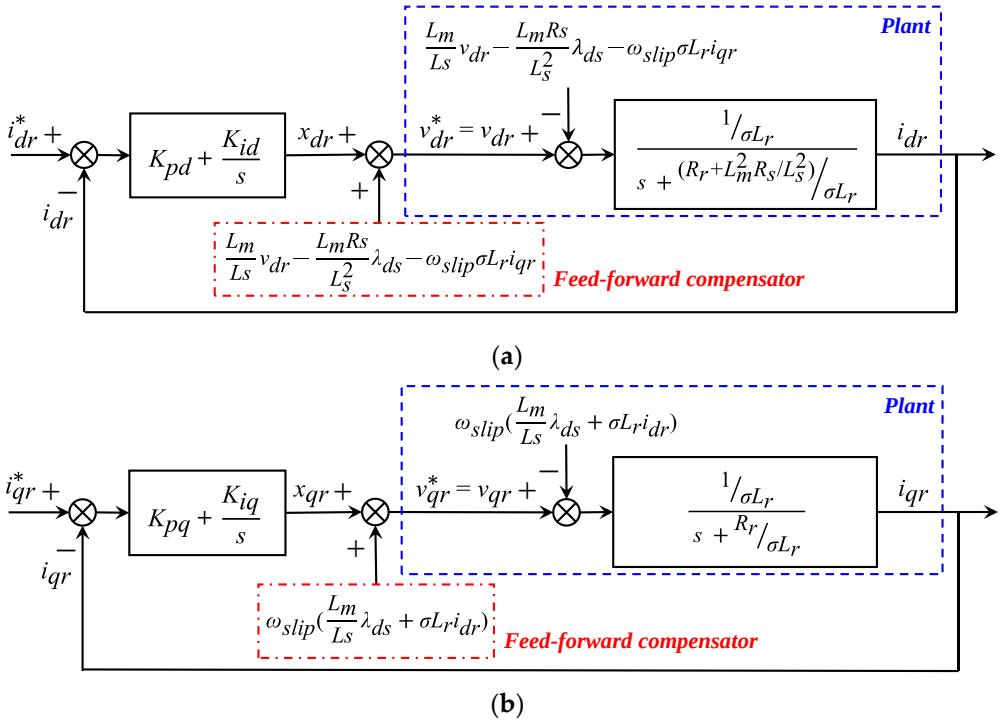

Figure 3. Rotor current regulators and feed-forward compensators. (**a**) d-axis current regulator. (**b**) q-axis current regulator.

2.2. Non-Linear Model of the Real and Reactive Power Controller

The commands for d-axis and q-axis current regulators, i^*_{dr} and i^*_{qr}, in Figure 3 are determined by the real and reactive power controller as described in Figure 4.

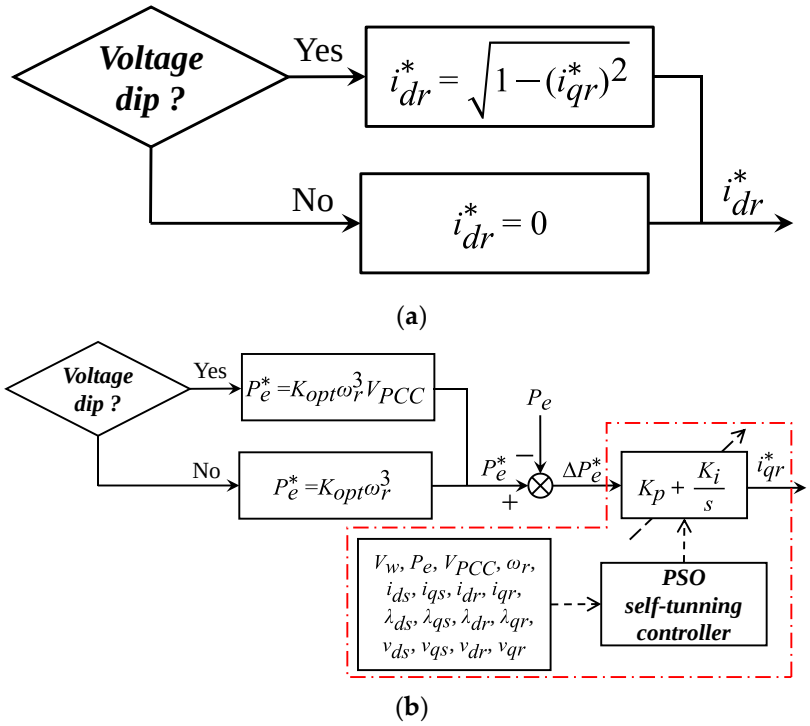

Figure 4. The proposed reactive and real power controller. (**a**) reactive power controller. (**b**) real power controller.

As shown in Figure 4, the real power output command P_e^* of the DFIG in normal operation is determined based on MPPT as follows [29]:

$$P_e^* = P_{e,opt}^* = K_{opt}\omega_r^3 \tag{4}$$

where K_{opt} is a constant. When there is a fault in the grid causing a voltage dip at *PCC* ($|V_{PCC}| \leq 0.8\ pu$), the real power output command P_e^* is decreased to a level proportional to the voltage at *PCC*, i.e.,

$$P_e^* = P_{e,opt}^* V_{PCC} = K_{opt}\omega_r^3 V_{PCC} \tag{5}$$

where V_{PCC} is the *PCC* voltage per unit. Based on the error ΔP_e^* between the real power output command P_e^* and the actual real power output P_e, a PI real power controller is proposed to generate the desired *q*-axis rotor current command i_{qr}^*. In order to improve the dynamic power and voltage responses under fault conditions, the gains of the PI real power controller are adapted in real time using PSO based on on-line measured wind speed V_w, real power P_e, *PCC* voltage V_{PCC}, rotor speed ω_r, stator and rotor currents, voltages, and flux linkages. Details on the design of the fixed-gain PI real power controller and PSO self-tuning controller will be described in the following sections.

It is also observed in Figure 4 that the *d*-axis rotor current command i_{dr}^* is usually set to be zero [29] in order for the DFIG to have the largest *q*-axis rotor current command i_{qr}^* and maximum real power output as the following constraint must be satisfied by the two rotor current commands i_{dr}^* and i_{qr}^*:

$$i_{dr}^{*\,2} + i_{qr}^{*\,2} \leq |i_{r,\max}|^2 = 1 \tag{6}$$

When there is a fault causing a voltage dip, the real power output command P_e^* and the resultant *q*-axis rotor current command i_{qr}^* are decreased and the *d*-axis rotor current command i_{dr}^* is increased to a level as described below:

$$i_{dr}^* = \sqrt{1 - (i_{qr}^*)^2} \tag{7}$$

Thus, by increasing the *d*-axis rotor current according to Equation (7), the DFIG reactive power output can be increased and the voltage at *PCC* can be improved under fault conditions.

3. Design of Fixed-Gain Real Power Controllers

3.1. Linearized Model of the DFIG Gain Real Power Controller

In the design of the fixed-gain real power controller, the non-linear power equation $P_e = T_e\omega_r$ is first linearized as follows:

$$\Delta P_e(s) = T_{e0}\Delta\omega_r(s) + \omega_{r0}\Delta T_e(s) \tag{8}$$

where the rotor speed deviation can be derived from the block diagram in Figure 2 as follows:

$$\Delta\omega_r(s) = \left(\frac{1}{2Hs + D}\right)(\Delta T_m(s) - \Delta T_e(s)) \tag{9}$$

The increment in mechanical torque can be estimated using the following formula:

$$\Delta T_m(s) = \frac{\partial T_m}{\partial \omega_r}\Delta\omega_r(s) = k\Delta\omega_r(s) \tag{10}$$

Note that the constant k can be estimated from the wind turbine mechanical torque using the curve fitting technique around the maximum power point [28].

The increment in stator flux linkage, $\Delta\lambda_{ds}$, can be derived from Equation (1) as follows:

$$\Delta\lambda_{ds}(s) = \frac{1}{s + \frac{R_s}{L_s}}\left(\Delta v_{ds}(s) + \frac{L_m}{L_s}R_s\Delta i_{dr}(s)\right) \tag{11}$$

The electromagnetic torque T_e can be expressed as follows:

$$T_e = \frac{L_m}{L_s} i_{qr}\lambda_{ds} \tag{12}$$

By linearizing the torque equation in Equation (12), we get the increment in electromagnetic torque as follows:

$$\Delta T_e(s) = \frac{L_m}{L_s}\lambda_{ds0}\Delta i_{qr}(s) + \frac{L_m}{L_s} i_{qr0}\Delta\lambda_{ds}(s) \tag{13}$$

From the block diagrams in Figure 3 for d-axis and q-axis current regulators, the following transfer functions can be derived:

$$\frac{\Delta i_{dr}(s)}{\Delta i^*_{dr}(s)} = \frac{(K_{pd+} + \frac{K_{id}}{s})\frac{1}{\sigma L_{rs}s + R_r + \frac{L_m^2 R_s}{L_s^2}}}{1 + (K_{pd+} + \frac{K_{id}}{s})\frac{1}{\sigma L_r s + R_r + \frac{L_m^2 R_s}{L_s^2}}} \tag{14}$$

$$\frac{\Delta i_{qr}(s)}{\Delta i^*_{qr}(s)} = \frac{(K_{pq+} + \frac{K_{iq}}{s})\frac{1}{\sigma L_r s + R_r}}{1 + (K_{pq+} + \frac{K_{iq}}{s})\frac{1}{\sigma L_r s + R_r}} \tag{15}$$

From Equation (7), we obtain:

$$2i^*_{dr0}\Delta i^*_{dr} + 2i^*_{qr0}\Delta i^*_{qr} = 0 \tag{16}$$

Therefore, the increment in d-axis rotor current command Δi^*_{dr} is related to the increment in q-axis rotor current command i^*_{qr} as follows:

$$\Delta i^*_{dr} = -\frac{i^*_{qr0}}{i^*_{dr0}}\Delta i^*_{qr} \tag{17}$$

Based on Equations (8)–(11) and (13)–(17), the complete linearized model of the DFIG real power controller can be depicted by the block diagram of Figure 5.

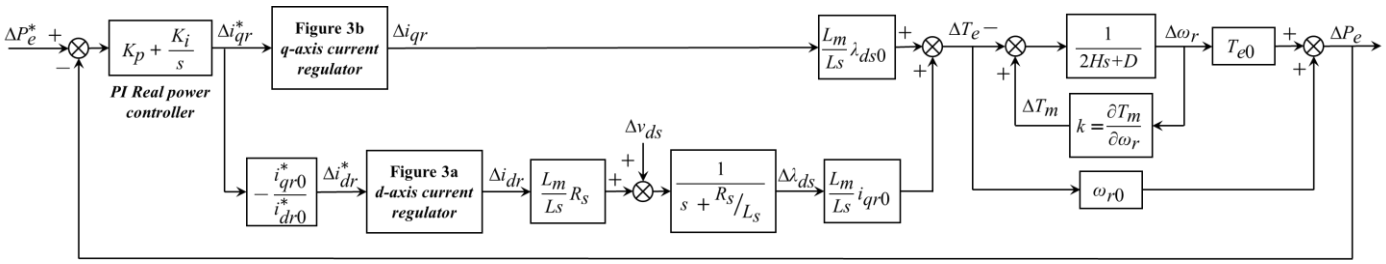

Figure 5. Block diagram of complete linearized model for DFIG real power controller.

3.2. Simplified Linear Model of the DFIG Real Power Controller

To compare the response speeds of the inner current regulator loop and outer power controller loop in Figure 2, the dynamic response curves to step changes in the inputs to the current regulator loop and power controller loop are compared in Figure 6a. Note that the current regulator gains were determined by using the method in [30]. It is observed from the response curves in Figure 6a that the rise time for the current regulator is about 0.1 s, which is much smaller than 5 s for the power controller. Thus, it is concluded that the response speed of the current regulator is much faster than the power controller.

In addition, only a very insignificant change in the dynamic response of the power controller is observed in Figure 6b when the transfer function of the current regulator is simplified to be unity as done in the simplified linearized model for power controller design.

When the change in stator flux linkage $\Delta\lambda_{ds}$ is neglected [29], the simplified linear model as shown in Figure 7 can be reached for DFIG real power control.

Details on the design of the gains K_p and K_i for the PI controller are described below.

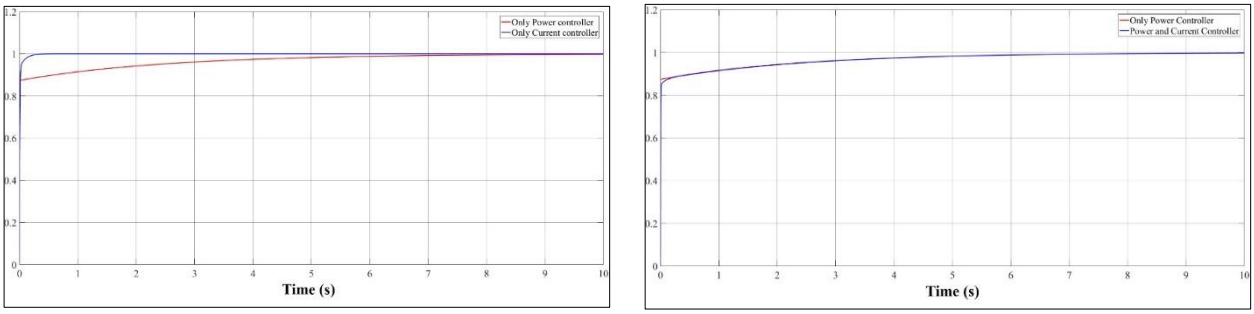

(**a**) (**b**)

Figure 6. Dynamic response curves of the power controller and current regulator. (**a**) Dynamic response curves to step inputs to the current regulator loop and power controller loop. (**b**) Dynamic response of the power controller with and without current controller.

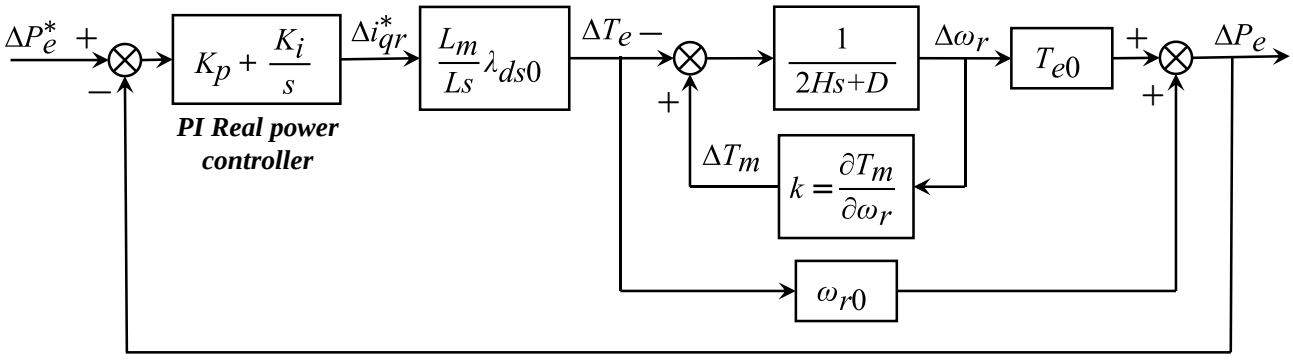

Figure 7. Simplified linear model for DFIG real power controller design.

3.3. Design of the Fixed-Gain Proportional-Integral (PI) Real Power Controller

The open-loop transfer function of Figure 7 can be expressed as:

$$G(s) = \frac{K_p(s + \frac{K_i}{K_p})}{s}(\frac{L_m\lambda_{ds0}}{L_s})(\frac{\omega_{r0}(2Hs + D - k) - T_{e0}}{2H(s + \frac{(D-k)}{2H})}) \quad (18)$$

To avoid oscillations and overshoots in a second order system, the gains of the PI controller, K_p and K_i, are selected as follows to achieve first-order system response through pole-zero cancellation:

$$\frac{K_i}{K_p} = \frac{D - k}{2H} \quad (19)$$

From Equations (18) and (19), the closed-loop transfer function is given by:

$$T(s) = \frac{G(s)}{1 + G(s)} = \frac{2HK_p\omega_{r0}(\frac{L_m\lambda_{ds0}}{L_s})s + K_p(\frac{L_m\lambda_{ds0}}{L_s})(\omega_{r0}(D - k) - K_pT_{e0})}{2H(1 + K_p\omega_{r0}(\frac{L_m\lambda_{ds0}}{L_s})s + K_p(\frac{L_m\lambda_{ds0}}{L_s})(\omega_{r0}(D - k) - T_{e0}))} \quad (20)$$

The proportional gain K_p can be determined from Equation (20) based on the selected bandwidth ω_p of $|T(s)|$. As evidenced by the response curves in Figure 6a, the response speed of the current regulator is much faster than that of the power controller. Therefore, the bandwidth ω_p of the power controller is chosen as follows:

$$\omega_p = 0.01\omega_i \quad (21)$$

where ω_i is the bandwidth of the current regulator as described below:

$$\omega_i = 7\omega_{slip} = 7slip \times \omega_e \quad (22)$$

where ω_e is the synchronous speed. The wind speed V_{w0}, rotor speed ω_{r0}, electromagnetic torque T_{e0}, the constants k, D, H, and the reached PI controller gains under the steady-state operating point are listed in Table 1.

Table 1. System constants and proportional-integral (PI) controller gains under the steady-state operating point.

V_{w0}	ω_{r0}	T_{e0}	k	D	H	K_p	K_i
11	0.9417	0.76	−0.845	0	1.75	1.181	0.2851

4. Design of Particle Swarm Optimization (PSO) Self-Tuning Controllers

As mentioned in the previous section, the gains K_p and K_i for the fixed-gain real power controller in Figure 7 have been determined based on a particular operating point. In other words, the gains K_p and K_i are functions of system variables such as q-axis rotor current i_{qr}, stator flux linkage λ_{ds}, rotor speed ω_r and electromagnetic torque T_e. Therefore, these controller gains must be updated based on the on-line measured system variables i_{qr}, λ_{ds}, ω_r, T_e, . . . , etc., in order to maintain best performance when there are significant changes in system variables due to a major disturbance such as a three-phase fault in the grid. In this paper, a PSO self-tuning controller as shown in Figure 4 is proposed in order to adapt the real power controller gains K_p and K_i in real-time. A better voltage profile can thus be achieved by the proposed PSO self-tuning controller than the fixed-gain PI controller.

The procedures to adjust the desired controller gains K_p and K_i followed by the proposed PSO self-tuning real power controller are summarized in Figure 8 [26–28]. The details of these procedures are described as follows.

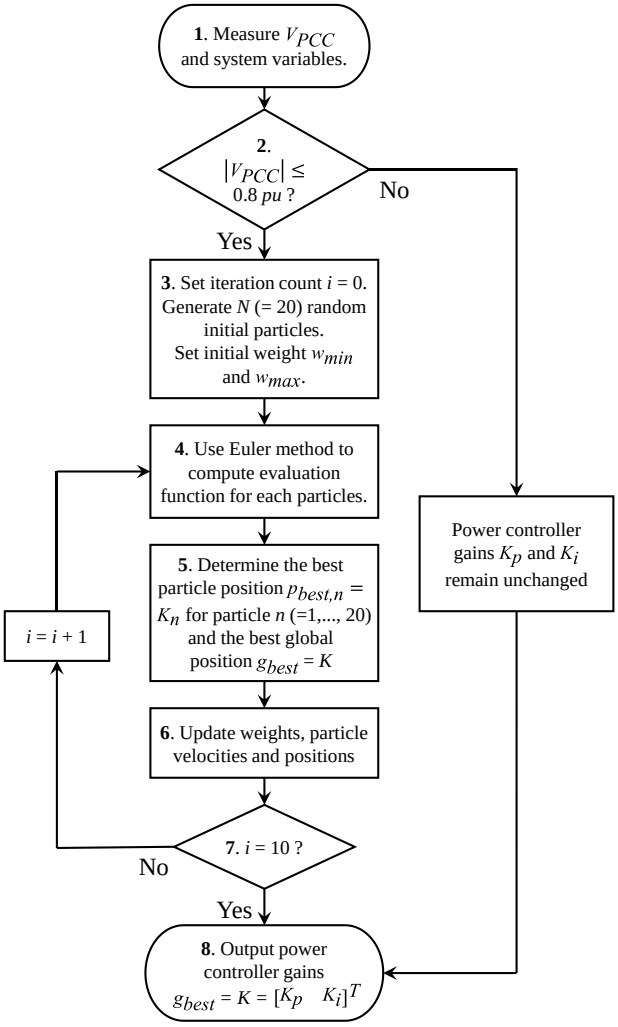

Figure 8. Flowchart for the procedure of adjusting gains K_p and K_i by particle swarm optimization (PSO) self-tuning real power controller.

Step (1): Measure *PCC* voltage V_{PCC}, wind speed V_w, rotor speed ω_r, stator currents i_{ds}, i_{qs}, rotor currents i_{dr}, i_{qr}, stator voltages v_{ds}, v_{qs}, rotor voltages v_{dr}, v_{qr}, stator flux linkages λ_{ds}, λ_{qs}, and rotor flux linkages λ_{dr}, λ_{qr} every 0.2 s.

Step (2): The PSO self-tuning controller is initiated when $|V_{PCC}| \leq 0.8\ pu$.

Step (3): Set initial iteration count $i = 0$. Generate N (= 20) random initial particles with position vector $K_n^{(0)} = \begin{bmatrix} K_{n,p}^{(0)} & K_{n,i}^{(0)} \end{bmatrix}^T$ and velocity vector $V_n^{(0)} = \begin{bmatrix} \Delta K_{n,p}^{(0)} & \Delta K_{n,i}^{(0)} \end{bmatrix}^T$ for particle n (=1,⋯, 20). Set initial weight $w_n^{(0)} = w_{\max} = 0.1$.

Step (4): Compute the evaluation function as defined below for each particle.

$$E = \int_0^{0.5} |P_e^* - P_e(t)|\, dt \cong \sum_{h=1}^{10} |P_e^* - P_e(t)|\Delta t \tag{23}$$

where $P_e(t)$ is the predicted real power in the future 0.5 s which can be estimated by the following equation:

$$P_e(t) = -(v_{ds}(t)i_{ds}(t) + v_{qs}(t)i_{qs}(t) + v_{dr}(t)i_{dr}(t) + v_{qr}(t)i_{qr}(t)) \tag{24}$$

A subroutine based on Euler method is developed to estimate the voltages and currents in Equation (24) in the future 0.5 s.

In order to make real power $P_e(t)$ as close to the desired value P_e^* as possible, the evaluation function is selected as the integral of $|P_e^* - P_e(t)|dt$ in the future 0.5 s, as shown in Equation (23).

Step (5): The best particle position is updated as $K_n = K_n^{(i)}$ when the evaluation function E for particle n with position $K_n^{(i)}$ at iteration i is less than that for the best particle position $p_{\text{best},n} = K_n$ for particle n. Otherwise, K_n remains unchanged. Let particle m ($1 \leq m \leq 20$) with position $K_m^{(i)}$ be the one with smallest evaluation function among the 20 particles at the i-th iteration. The best global position, K, is updated as $K = K_m^{(i)}$ at the i-th iteration if $E(K_m^{(i)}) < E(K)$. Otherwise, K remains unchanged.

Step (6): Update weights, particle velocities, and particle positions for the next iteration using the following Equations (25)–(27):

$$w_n^{(i)} = w_{\max} - \frac{w_{\max} - w_{\min}}{M} i \tag{25}$$

$$V_n^{(i+1)} = w_n^{(i)} V_n^{(i)} + r_1(K_n - K_n^{(i)}) + r_2(K - K_n^{(i)}) \tag{26}$$

$$K_n^{(i+1)} = K_n^{(i)} + V_n^{(i+1)} \tag{27}$$

where $w_{\max} = 0.1$, $w_{\min} = 0.01$, $M = 10$, and r_1 and r_2 are random numbers between 0 and 1.

Step (7) and (8): The PSO algorithm is repeated for M (= 10) iterations in order to reach the desired optimal power controller gains $g_{best} = K = \begin{bmatrix} K_p & K_i \end{bmatrix}^T$.

5. Simulation Results

To demonstrate the effectiveness of the proposed PSO self-tuning real power, the dashed position of the system in Figure 1 was simulated using MATLAB/SIMULINK. The parameters for the DFIG are given in the Nomenclature. The simulated dynamic responses of the wind farm subject to a three-phase fault at point "Fault" in Figure 1 are presented as follows. As the settling time reduces with increasing integral gain K_i, the gain K_i for the fixed-gain PI controller in Table 1 was tripled in the simulations in order to reduce the simulation time.

5.1. Dynamic Responses for a Fault Voltage of 0.5 pu

Figure 9 compares the dynamic response curves by using MPPT operation mode and by using the proposed de-loaded power control method with fixed-gain PI controller when the wind farm is subject to a three-phase fault at the *PCC* causing a voltage drop from 1 *pu* to 0.5 *pu*.

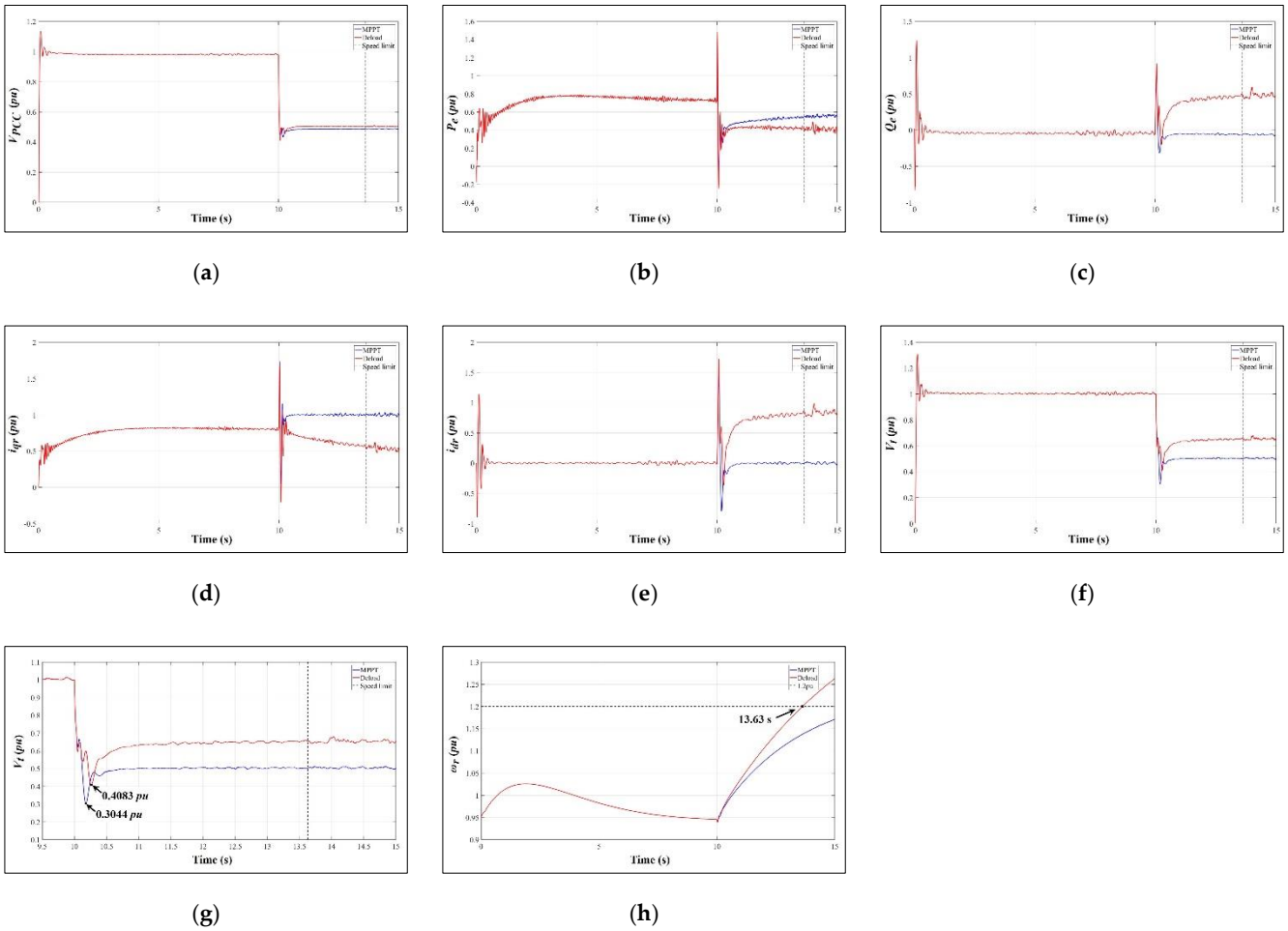

(**a**) (**b**) (**c**)

(**d**) (**e**) (**f**)

(**g**) (**h**)

Figure 9. Dynamic response curves for maximum power point tracking (MPPT) operation mode and fixed-gain PI de-loaded controller when the grid is subject to a fault of 0.5 *pu*. (**a**) Voltage at *PCC*. (**b**) Wind farm real power. (**c**) Wind farm reactive power. (**d**) *q*-axis rotor current. (**e**) *d*-axis rotor current. (**f**) Wind farm terminal voltage. (**g**) Enlarged version of the terminal voltage. (**h**) Generator speed.

Based on the response curves in Figure 9, the following observations are in order:

(1) When a low voltage due to a fault is detected at t = 10 s, the real power in Figure 9b for the de-loaded control method with fixed-gain PI controller is reduced by 50% according to Equation (5) through the reduction in *q*-axis rotor current i_{qr} as shown in Figure 9d. According to Equation (7), the *d*-axis rotor current i_{dr} in Figure 9e can be increased as a result of the decrease in i_{qr}. Thus, the reactive power in Figure 9c is increased and the wind farm terminal voltage in Figure 9f is improved.

(2) To compare wind farm terminal voltages from the proposed fixed-gain PI de-loaded controller and MPPT operation mode, the dynamic voltage response curves in Figure 9f are enlarged and depicted in Figure 9g. It is observed from Figure 9g that the lowest voltage from the MPPT operation mode is 0.3044 *pu* while that from the fixed-gain PI de-loaded controller is 0.4083 *pu*. The lowest voltage is improved by 34.13% when MPPT operation mode is replaced by the fixed-gain de-loaded controller during the faulted period.

Figure 10 compares the dynamic response curves of the wind farm with fixed-gain PI de-loaded controller and PSO self-tuning controller when the grid is subject to a fault of 0.5 *pu*. Based on the response curves in Figure 10, the following observations can be made:

(1) To compare the wind farm terminal voltages from the proposed fixed-gain PI de-loaded controller and PSO controller in Figure 4, the dynamic voltage response curves

in Figure 10f are enlarged and depicted in Figure 10g. It is observed from Figure 10g that the lowest voltage from the fixed-gain PI controller is 0.4083 *pu* while that from the PSO controller is improved to 0.4759 *pu*. A 16% improvement in the lowest voltage can be achieved by the proposed PSO controller than the fixed-gain PI controller.

(2) The PSO self-tuning controller can yield a better voltage response than the fixed-gain PI controller since its gains K_p and K_i are updated in real time every 0.2 s based on on-line measurements, as shown in Figure 10i.

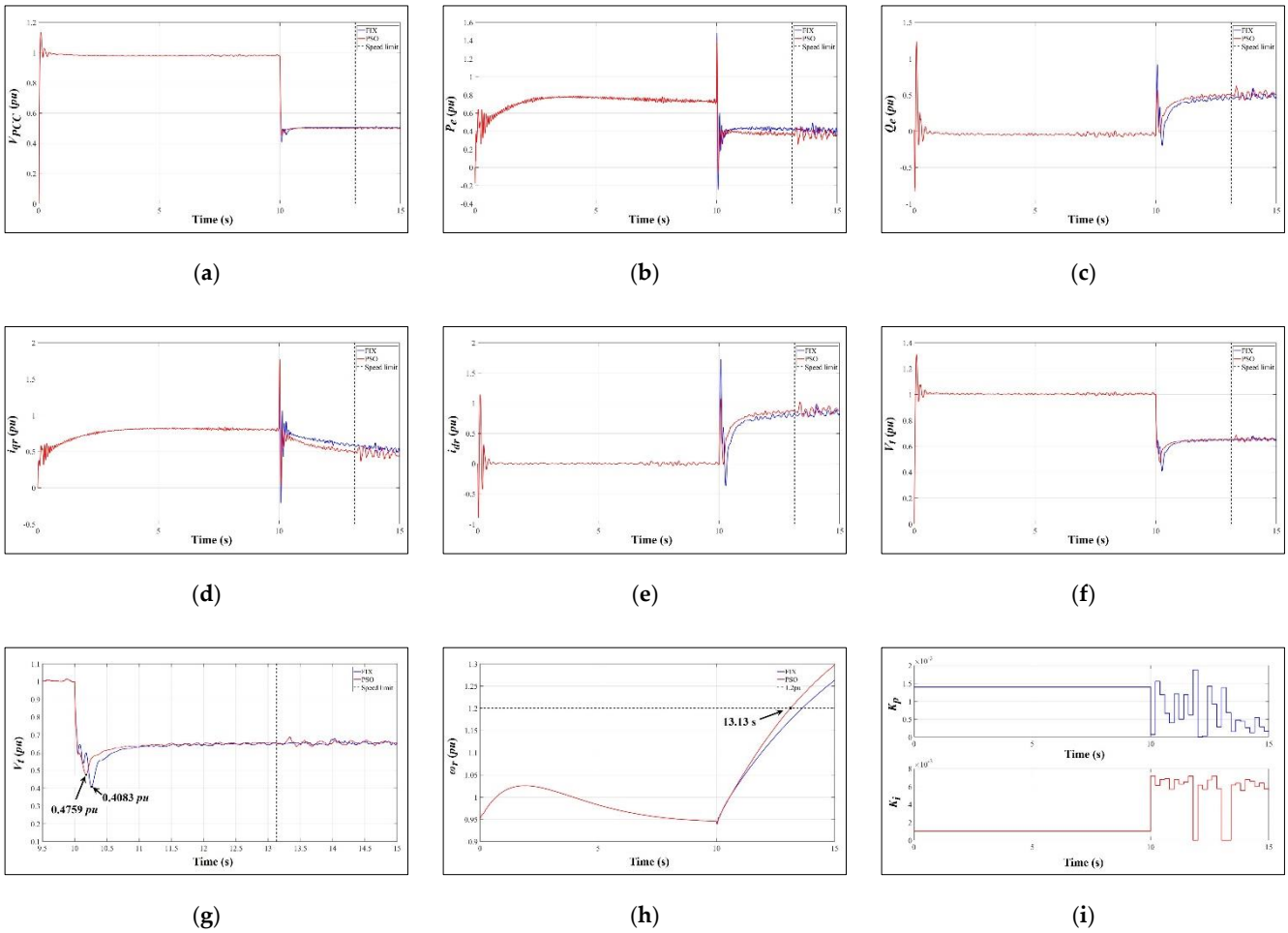

Figure 10. Dynamic response curve for fixed-gain PI de-loaded controller and PSO self-tuning de−loaded controller when the grid is subject to a fault of 0.5 *pu*. (**a**) Voltage at point of common coupling (*PCC*). (**b**) Wind farm real power. (**c**) Wind farm reactive power. (**d**) *q*-axis rotor current. (**e**) *d*-axis rotor current. (**f**) Wind farm terminal voltage. (**g**) Enlarged version of the terminal voltage. (*h*) Generator rotor speed. (**i**) PSO controller gains K_p and K_i.

As the real power output is decreased in the proposed de-loaded power controller in Figure 4 in order to increase the reactive power output and to improve wind farm terminal voltage, generator speed increases during the faulted period. It is thus essential to ensure that the wind farm meets the LVRT requirement set by the local utility (Taiwan Power Company) as depicted in Figure 11.

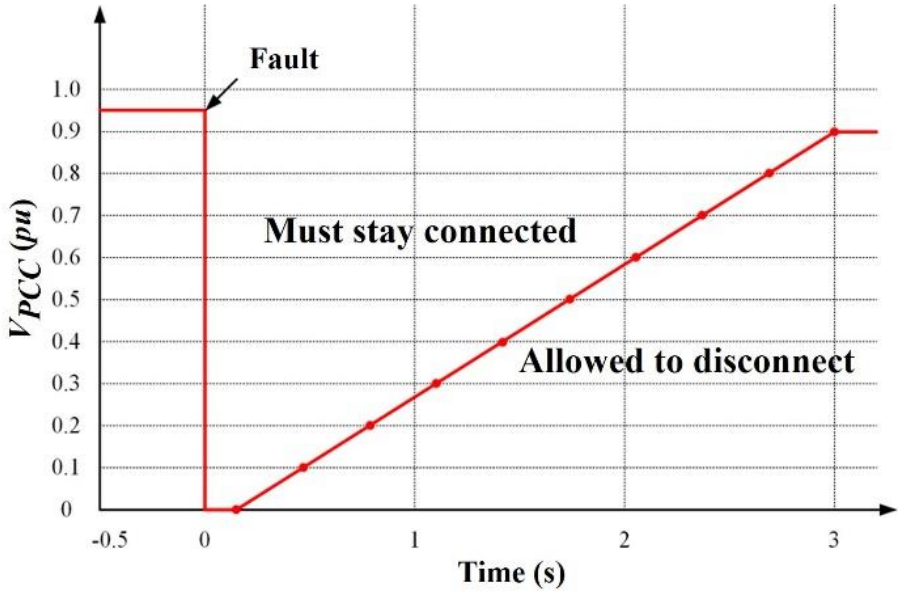

Figure 11. Low voltage ride through (LVRT) curve for Taiwan Power Company.

It is observed from Figure 10h that the generator exceeds the speed limit of 1.2 *pu* at t = 13.63 s and t = 13.13 s, respectively, for the proposed fixed-gain PI controller and PSO self-tuning controller. This means that the wind farm will remain in a stable operation for a period of 3.63 s and 3.13 s for the fixed-gain controller and self-tuning PI controller, respectively.

Since the required operation time for a fault voltage level of 0.5 *pu* in Figure 11 is 1.733 s, it is concluded that both the proposed fixed-gain PI controller and the proposed PSO self-tuning controller meet the LVRT requirement.

5.2. Dynamic Responses for a Fault Voltage of 0.3 pu

To examine the effectiveness of the proposed fixed-gain PI controller and PSO self-tuning controller under very low grid voltage, the dynamic responses for the wind farm subject to a 0.3 *pu* fault voltage at *PCC* were simulated using MATLAB/SIMULINK and the results are illustrated in Figure 12.

It is observed from Figure 12g that the lowest voltage from the fixed-gain PI controller is 0.2291 *pu* while that from the PSO controller is improved to 0.2846 *pu*. A 24.23% improvement in the lowest voltage has been achieved by the proposed PSO controller than the fixed-gain PI controller.

It is also observed from Figure 12h that the durations for the generator to run within the speed limit of 1.2 *pu* are 2.4 s and 2.18 s for the wind farm with fixed-gain PI controller and PSO self-tuning controller, respectively. Since the minimal operation time is 1.1 s from Figure 11, both controllers meet the LVRT requirement.

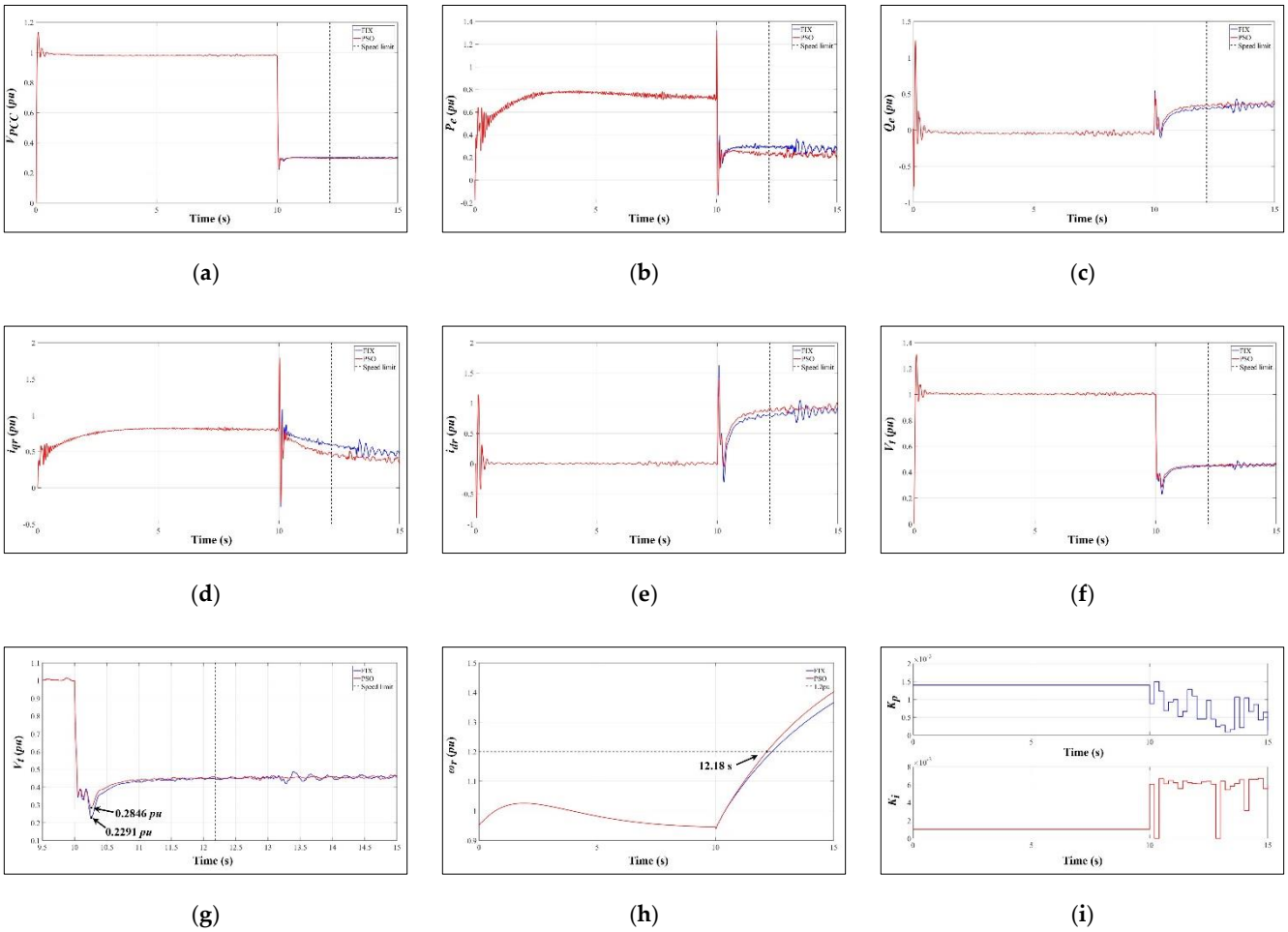

(**a**) (**b**) (**c**)

(**d**) (**e**) (**f**)

(**g**) (**h**) (**i**)

Figure 12. Dynamic response curves for a fault voltage of 0.3 *pu*. (**a**) Voltage at *PCC*. (**b**) Wind farm real power. (**c**) Wind farm reactive power. (**d**) $q-$axis rotor current. (**e**) $d-$axis rotor current. (**f**) Wind farm terminal voltage. (**g**) Enlarged version of the terminal voltage. (**h**) Generator rotor speed. (**i**) PSO controller gains K_p and K_i.

6. Conclusions

To improve the wind farm terminal voltage and to provide reactive power support to the system under grid fault situations, a de-loaded real power control strategy implemented with both a fixed-gain PI controller and a PSO self-tuning controller has been proposed. The effectiveness of the proposed de-loaded real power control strategy has been demonstrated on an offshore wind farm in Taiwan using MATLAB/SIMULINK simulations. Specific conclusions are as follows:

(1) When the wind farm is subject to a grid fault, the wind farm terminal voltage drops to a very low level if the wind farm remains in MPPT operation mode. The terminal voltage can be improved if the wind farm is operated using the proposed real power de-loaded control strategy with a fixed-gain PI controller. The reactive power output of the wind farm can also be increased. Further improvement in voltage profile can be achieved if the fixed-gain PI controller is replaced by the proposed PSO self-tuning controller.

(2) Since the improvement in voltage profile is achieved by increasing reactive power output and decreasing real power output, generator speed will increase at a higher rate than that in the MPPT operation mode. In addition, the de-loaded strategy with a PSO self-tuning controller, which gives a better voltage profile than that with a fixed-gain PI controller, has a higher rate of increase in generator speed and a shorter duration for the generator to operate within the speed limit of 1.2 *pu*. However, the LVRT requirement is met by both the fixed gain and PSO controllers.

(3) Future works will be devoted to the coordination of pitch angle controller and de-loaded strategy in order to improve the voltage profile and duration of stable operation further.
(4) Only the design of the rotor side converter is investigated in this work. Proper design of the grid side converter may help improve the voltage profile.
(5) Only LVRT is studied in this work. The high-voltage ride through (HVRT) will be investigated in future works.

Author Contributions: Conceptualization, methodology, validation and investigation, Y.-H.H. Writing—review and editing, visualization, Y.-W.C. Writing—review and editing, visualization, C.-H.C. writing—original draft, supervision, and project administration, Y.-Y.H. All authors have read and agreed to the published version of the manuscript.

Funding: This work was supported by the Ministry of Science and Technology of Taiwan, under contract MOST 106-2221-E-002-147-MY3.

Conflicts of Interest: The authors declare that they have no known competing financial interests or personal relationships that could have appeared to influence the work reported in this paper.

Nomenclature

D	Damping coefficient
H	Inertia time constant
i_{ds}, i_{qs}	d-axis and q-axis stator currents
i_{dr}, i_{qr}	d-axis and q-axis rotor currents
i_{dr}^*, i_{qr}^*	The commands for d-axis and q-axis current regulators
K_p, K_i	Proportional and integral gains of real power controller
L_s, L_r, L_m	Stator, rotor, and magnetizing inductances
P_e^*, P_e	Real power output command and actual real power output
R_s, R_r	Stator and rotor resistances
T_m, T_e	Mechanical torque and electromagnetic torque
V_{PCC}	Voltage at the point of common coupling
V_w	Wind speed
v_{ds}, v_{qs}	d-axis and q-axis stator voltages
v_{dr}, v_{qr}	d-axis and q-axis rotor voltages
λ_{ds}, λ_{qs},	d-axis and q-axis stator flux linkages
ω_r	Rotor speed

References

1. Liu, W.; Wu, Y.; Lee, C.; Chen, C. Effect of low-voltage-ride-through technologies on the first Taiwan offshore wind farm planning. *IEEE Trans. Sustain. Energy* **2011**, *2*, 78–86. [CrossRef]
2. López, J.; Sanchis, P.; Roboam, X.; Marroyo, L. Dynamic behavior of the doubly fed induction generator during three-phase voltage dips. *IEEE Trans. Energy Convers.* **2007**, *22*, 709–717. [CrossRef]
3. López, J.; GubÍa, E.; Sanchis, P.; Roboam, X.; Marroyo, L. Wind turbines based on doubly fed induction generator under asymmetrical voltage dips. *IEEE Trans. Energy Convers.* **2008**, *23*, 321–330. [CrossRef]
4. Marques, G.D.; Sousa, D.M. Understanding the doubly fed induction generator during voltage dips. *IEEE Trans. Energy Convers.* **2012**, *27*, 421–431. [CrossRef]
5. Pannell, G.; Atkinson, D.J.; Zahawi, B. Minimum-threshold crowbar for a fault-ride-through grid-code-compliant DFIG wind turbine. *IEEE Trans. Energy Convers.* **2010**, *25*, 750–759. [CrossRef]
6. López, J.; GubÍa, E.; Olea, E.; Ruiz, J.; Marroyo, L. Ride through of wind turbines with doubly fed induction generator under symmetrical voltage dips. *IEEE Trans. Ind. Electron.* **2009**, *56*, 4246–4254. [CrossRef]
7. Pannell, G.; Zahawi, B.; Atkinson, D.J.; Missailidis, P. Evaluation of the performance of a DC-link brake chopper as a DFIG low-voltage fault-ride-through device. *IEEE Trans. Energy Convers.* **2013**, *28*, 535–542. [CrossRef]
8. Yang, J.; Fletcher, J.E.; O'Reilly, J. A series-dynamic-resistor-based converter protection scheme for doubly-fed induction generator during various fault conditions. *IEEE Trans. Energy Convers.* **2010**, *25*, 422–432. [CrossRef]
9. Zhang, S.; Tseng, K.; Choi, S.S.; Nguyen, T.D.; Yao, D.L. Advanced control of series voltage compensation to enhance wind turbine ride through. *IEEE Trans. Power Electron.* **2012**, *27*, 763–772. [CrossRef]
10. Okedu, K.E.; Muyeen, S.M.; Takahashi, R.; Tamura, J. Wind farms fault ride through using DFIG with new protection scheme. *IEEE Trans. Sustain. Energy* **2012**, *3*, 242–254. [CrossRef]

11. Yan, X.; Venkataramanan, G.; Wang, Y.; Dong, Q.; Zhang, B. Grid-fault tolerant operation of a DFIG wind turbine generator using a passive resistance network. *IEEE Trans. Power Electron.* **2011**, *26*, 2896–2905. [CrossRef]
12. Yan, X.; Venkataramanan, G.; Flannery, P.S.; Wang, Y.; Dong, Q.; Zhang, B. Voltage-sag tolerance of DFIG wind turbine with a series grid side passive-impedance network. *IEEE Trans. Energy Convers.* **2010**, *25*, 1048–1056. [CrossRef]
13. Huang, P.; Moursi, M.S.E.; Hasen, S.A. Novel fault ride-through scheme and control strategy for doubly fed induction generator-based wind turbine. *IEEE Trans. Energy Convers.* **2015**, *30*, 635–645. [CrossRef]
14. Ibrahim, A.O.; Nguyen, T.H.; Lee, D.; Kim, S. A fault ride-through technique of DFIG wind turbine systems using dynamic voltage restorers. *IEEE Trans. Energy Convers.* **2011**, *26*, 871–882. [CrossRef]
15. Wessels, C.; Gebhardt, F.; Fuchs, F.W. Fault ride-through of a DFIG wind turbine using a dynamic voltage restorer during symmetrical and asymmetrical grid faults. *IEEE Trans. Power Electron.* **2011**, *26*, 807–815. [CrossRef]
16. Abdel-Baqi, O.; Nasiri, A. Series voltage compensation for DFIG wind turbine low-voltage ride-through solution. *IEEE Trans. Energy Convers.* **2011**, *26*, 272–280. [CrossRef]
17. Amalorpavaraj, R.A.J.; Kaliannan, P.; Padmanaban, S.; Subramaniam, U.; Ramachandaramurthy, V.K. Improved fault ride through capability in DFIG based wind turbines using dynamic voltage restorer with combined feed-forward and feed-back control. *IEEE Access* **2017**, *5*, 20494–20503. [CrossRef]
18. Ambati, B.; Kanjiya, P.; Khadkikar, V. A low component count series voltage compensation scheme for DFIG WTs to enhance fault ride-through capability. *IEEE Trans. Energy Convers.* **2015**, *30*, 208–217. [CrossRef]
19. Kanjiya, P.; Ambati, B.B.; Khadkikar, V. A novel fault-tolerant DFIG-based wind energy conversion system for seamless operation during grid faults. *IEEE Trans. Power Syst.* **2014**, *29*, 1296–1305. [CrossRef]
20. Flannery, P.; Venkataramanan, G. Unbalanced voltage sag ride-through of a doubly fed induction generator wind turbine with series grid side converter. In Proceedings of the 2008 IEEE Industry Applications Annual Meeting, Edmonton, AB, Canada, 5–9 October 2008; pp. 1–8. [CrossRef]
21. Flannery, P.S.; Venkataramanan, G. A fault tolerant doubly fed induction generator wind turbine using a parallel grid side rectifier and series grid side converter. *IEEE Trans. Power Electron.* **2008**, *23*, 1126–1135. [CrossRef]
22. Zhu, R.; Chen, Z.; Wu, X.; Deng, F. Virtual damping flux-based LVRT control for DFIG-based wind turbine. *IEEE Trans. Energy Convers.* **2015**, *30*, 714–725. [CrossRef]
23. Yang, L.; Xu, Z.; Ostergaard, J.; Dong, Z.Y.; Wong, K.P. Advanced control strategy of DFIG wind turbines for power system fault ride through. *IEEE Trans. Power Syst.* **2012**, *27*, 713–722. [CrossRef]
24. Mokryani, G.; Siano, P.; Piccolo, A.; Chen, Z. Improving fault ride- through capability of variable speed wind turbines in distribution networks. *IEEE Syst. J.* **2013**, *7*, 713–722. [CrossRef]
25. Vieira, J.P.A.; Nunes, M.V.A.; Bezerra, U.H.; do Nascimento, A.C. Designing optimal controllers for doubly fed induction generators using a genetic algorithm. *IET Gener. Transm. Distrib.* **2009**, *3*, 472–484. [CrossRef]
26. Kennedy, J.; Eberhart, R. Particle swarm optimization. In Proceedings of the ICNN'95-International Conference on Neural Networks, Perth, WA, Australia, 27 November–1 December 1995; Volume 1944, pp. 1942–1948.
27. Kennedy, J.; Eberhart, R. A new optimizer using particle swarm theory. In Proceedings of the MHS'95 Sixth International Symposium on Micro Machine and Human Science, Nagoya, Japan, 4–6 October 1995; pp. 39–43.
28. Yang, J.S.; Chen, Y.W.; Hsu, Y.Y. Small-signal stability analysis and PSO self-tuning frequency control for an islanding system with DFIG wind farm. *IET Gener. Transm. Distrib.* **2019**, *13*, 563–574. [CrossRef]
29. Pena, R.; Clare, J.C.; Asher, G.M. Doubly fed induction generator using back-to-back PWM converters and its application to variable-speed wind-energy generation. *IEE Proc. Electr. Power Appl.* **1996**, *143*, 231–241. [CrossRef]
30. Weng, Y.T.; Hsu, Y.Y. Sliding mode regulator for maximum power tracking and copper loss minimisation of a doubly fed induction generator. *IET Renew. Power Gener.* **2015**, *9*, 297–305. [CrossRef]